

# PoIFusion: Multi-Modal 3D Object Detection via Fusion at Points of Interest

Jiajun Deng<sup>1</sup>, Sha Zhang<sup>2,3</sup>, Feras Dayoub<sup>1</sup>, Wanli Ouyang<sup>3</sup>, Yanyong Zhang<sup>2</sup>, Ian Reid<sup>1,4</sup>

<sup>1</sup> The University of Adelaide, Australian Institute for Machine Learning

<sup>2</sup> University of Science and Technology of China

<sup>3</sup> Shanghai Artificial Intelligent Laboratory <sup>4</sup> Mohamed bin Zayed University of AI

## Abstract

In this work, we present *PoIFusion*, a simple yet effective multi-modal 3D object detection framework to fuse the information of RGB images and LiDAR point clouds at the point of interest (abbreviated as *PoI*). Technically, our *PoIFusion* follows the paradigm of query-based object detection, formulating object queries as dynamic 3D boxes. The *PoIs* are adaptively generated from each query box on the fly, serving as the keypoints to represent a 3D object and play the role of basic units in multi-modal fusion. Specifically, we project *PoIs* into the view of each modality to sample the corresponding feature and integrate the multi-modal features at each *PoI* through a dynamic fusion block. Furthermore, the features of *PoIs* derived from the same query box are aggregated together to update the query feature. Our approach prevents information loss caused by view transformation and eliminates the computation-intensive global attention, making the multi-modal 3D object detector more applicable. We conducted extensive experiments on the *nuScenes* dataset to evaluate our approach. Remarkably, our *PoIFusion* achieves 74.9% NDS and 73.4% mAP, setting a state-of-the-art record on the multi-modal 3D object detection benchmark. Codes will be made available via <https://djjajunustc.github.io/projects/poifusion>.

## 1. Introduction

Autonomous vehicles are usually equipped with an array of sensors to facilitate safe driving, among which cameras and LiDARs are the most popular. These two sensors are complementary to each other: cameras provide rich textual and color information, while LiDAR sensors supply precise spatial measurements. The effective camera-LiDAR data fusion is widely regarded as a promising direction to achieve high-quality 3D object detection [2, 34, 42, 64], which has attracted a surge of research interest in the community.

The fundamental challenge of camera-LiDAR data fusion arises from the discrepancy of their representation

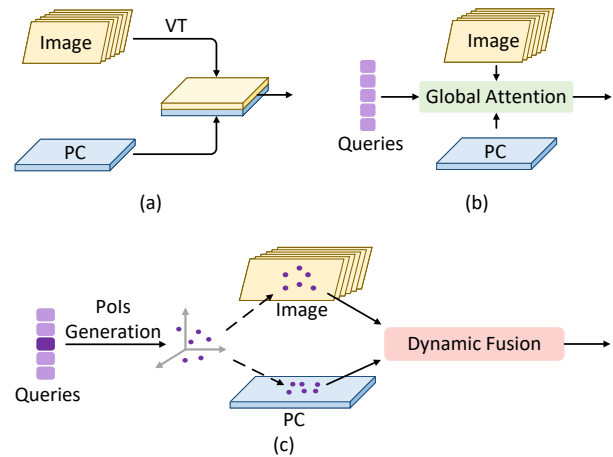


Figure 1. A comparison of (a) fusion with unified view, (b) fusion with global attention, and (c) our *PoIFusion*. “VT” and “PC” indicate view transformation and point clouds, respectively.

space (*i.e.*, 2D perspective view versus 3D space). To ameliorate this challenge, one common solution is to transform the image and point cloud representations into a unified bird-eye view [22, 34, 42], as depicted in Figure 1(a), or into 3D space [29]. Another recent approach [2, 69], as shown in Figure 1(b), keeps the representation in its original view and abstracts multi-modal features into object queries [6, 40] with the global attention mechanism [56].

However, both of these approaches have inherent issues. In the unified-view approach, the core component, *i.e.*, view transformation, is often based on monocular depth estimation to lift the 2D image into 3D. However, depth estimation is an error-prone task, with errors having a deleterious effect on any downstream tasks (such as object recognition). Moreover, the direct grid-to-grid fusion [34, 42] loses a significant portion of the original representational strengths which comprises modal-specific information [75].

The second query-based approach can avoid feature ambiguity and information loss by keeping the original view of the feature representation. However, the adoption of global attention to integrating multi-modal features incurs

high computation and memory overhead. For instance, the state-of-the-art algorithm [69], which follows the query-based approach of fusion with global attention, relies on the well-optimized Flash Attention operator [15] to cut down the time and memory consumption. The high overhead has become an obstacle that hinders the wide application of the algorithm. Furthermore, it is difficult to extract the object-relevant feature with the global attention mechanism [21, 84], especially when it comes to such a large 3D space like the autonomous driving scenario.

The benefit of the query-based approach inspires us to preserve the original view of features from each modality, while the above two issues motivate our exploration of an alternative paradigm to replace dense feature interaction of the global attention with sparse point projection and feature sampling, as illustrated in Figure 1(c).

As such, we propose a new query-based multi-modal 3D object detection framework that initializes object queries as learnable 3D boxes and dynamically integrates multi-modal features at representative points derived from each object query. In this manuscript, these representative points are referred to as **Points of Interest (PoIs)**, and our framework is named **PoIFusion**. Intuitively, a naive way to represent a 3D query box with points is to use the center point [8, 40, 69]. However, simply representing a 3D box with its center point totally ignores the geometric properties, such as the size and rotation angle. For supplementary, an improved design is to involve the corners [49]. Nevertheless, sampling multi-modal features according to the projected location of center and corner points also incurs the problem of feature misalignment, since the projection of a 3D box may not be a tight bounding box onto the image view. The issue remains even if a box is well-located in the 3D space [5], not to mention that the query box is not guaranteed to be accurately localized. To ameliorate this problem, our PoIs are adaptively generated from the center and corner points, with box-level and point-level transformation parameters online predicted according to the query feature. In our design, a single PoI serves as the basic unit for fine-grained multi-modal feature fusion, and the ensemble of PoIs derived from the same object query represents the regional feature in a flexible way.

Once PoIs are generated, the features from different modalities can be easily obtained by projecting PoIs onto the corresponding view, followed by bilinear interpolation according to the projected location. Moreover, because different modalities contribute differently to each object query, a dynamic fusion block is engaged in our design. Particularly, in our dynamic fusion block, we first generate the parameters of the fusion layer on the fly, and then integrate the sampled multi-modal feature at each PoI. The proposed adaptive PoIs, together with the dynamic fusion block, enable our PoIFusion to efficiently sample the object-relevant

multi-modal features and make the best of modal-specific information, thus improving 3D object detection.

We benchmark the proposed PoIFusion framework on the nuScene dataset and conduct extensive experiments to validate our designs. Notably, our method sets a new record on this challenging dataset, achieving 74.9% NDS and 73.4% mAP on the test set without bells and whistles.

In summary, our contributions are three-fold:

- We propose a novel PoIFusion framework for multi-modal 3D object detection that preserves modality-specific representation spaces while efficiently extracting and fusing features through sparse interactions.
- We present the design of fusion at points of interest, conveying an elegant view that the entity involved in the fusion module can be very flexible.
- We conduct extensive experiments to validate the effectiveness of our method, demonstrating its potential to serve as a strong baseline for future investigation.

## 2. Related Work

**LiDAR-Based 3D Object Detection.** LiDAR sensors capture 3D point clouds, which provide accurate spatial information that can be important for 3D object detection. Broadly, 3D object detection algorithms operated on point clouds can be categorized into two groups: point-based and voxel-based ones. Point-based 3D object detection algorithms [51, 73, 74] make direct use of the precise coordinates of points, progressively sampling keypoints and extracting local information with set abstraction operators [46, 47, 52, 53] that aggregate information from a point and its neighbours. In contrast, voxel-based 3D object detection algorithms [16, 17, 20, 28, 50, 72, 76, 80] first “voxelize” the point cloud by binning points into a regular grid. The voxel representation enables straightforward feature extraction using standard (or sparse) convolutions [9, 10, 70] or sparse voxel Transformers [12, 18, 19, 27, 44, 59, 81].

**Camera-Based 3D Object Detection.** 3D object detection is one of the oldest Computer Vision problems and a variety of approaches have been proposed over many years (we do not survey these here). For the purposes of 3D object detection from a moving car a popular approach, and one that can be readily fused with point-cloud estimates, is to measure detection success in the Birds-eye View (BEV) space. Earlier attempts along these lines – *e.g.*, geometric uncertainty [43] and pseudo-LiDAR representation [62] – mainly focus on monocular 3D object detection [3, 14, 48, 61, 79]. Autonomous driving vehicles are typically equipped with multiple cameras, providing perception information over the full 360 degrees. To leverage the relationship between multi-view images, BEV-based and query-based algorithms have been explored. BEV-based 3D object detection [25, 32, 33, 71] explicitly per-

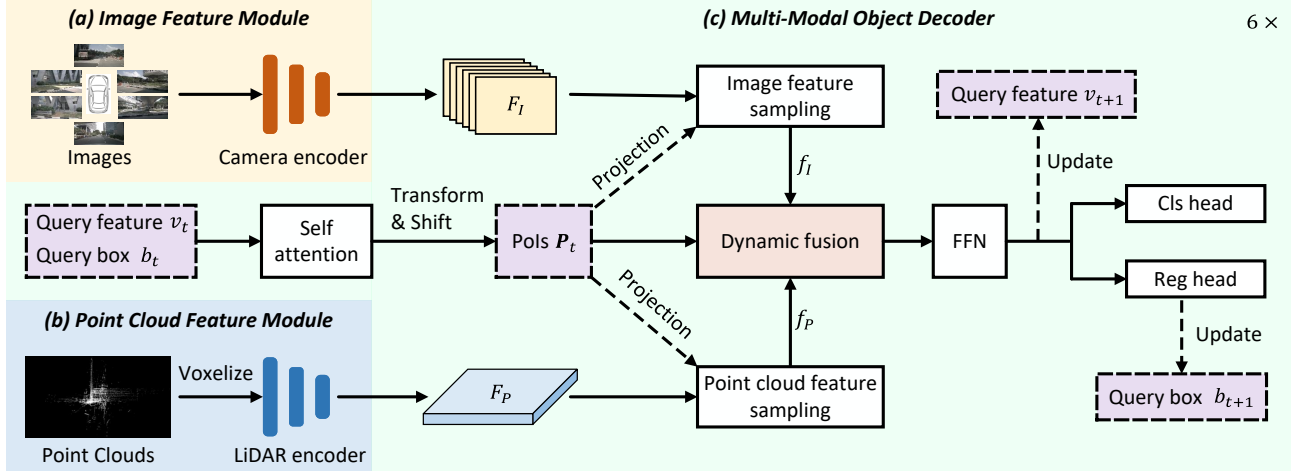


Figure 2. An overview of our proposed PoIFusion framework, which is mainly composed of (a) an image feature module, (b) a point cloud feature module, and (c) a multi-modal object decoder. In our PoIFusion, we independently extract the feature of each modality and keep the original representation view (*i.e.*, image feature in the perspective view, and point cloud feature in the bird-eye view). The multi-modal feature maps are taken as the input of our multi-modal object decoder. The object decoder is iteratively applied 6 times to integrate the multi-modal feature sampled by generated points of interest (PoIs) and refine the object queries.

forms view transformation to unify multi-view images into bird-eye-view representation. Query-based 3D object detection [38, 40, 54, 63, 65, 68] follows the pipeline of DETR [6], capitalizing on learnable object queries to extract multi-view information without view transformation.

**Multi-Modal 3D Object Detection.** Although the exploration of each individual modality has made encouraging progress, the accuracy and robustness of detection algorithms are still insufficient for safe driving. The fact that images and point clouds are naturally complementary to each other (*i.e.*, rich semantic information versus precise spatial information) has motivated further exploration in multi-modal 3D object detection [2, 8, 22, 26, 31, 60, 67]. In the early stage, the multi-modal approaches utilize point clouds as the principal component, introducing image features at the point level [13, 57, 58, 77] or proposal level [7, 78, 83] to enhance the features of the point clouds. Recently, inspired by multi-view 3D object detection, a series of works [29, 34, 42] propose that unifying the representation space with explicit view transformation [45] facilitates multi-modal fusion. Another group of methods [2, 30, 69, 75] leverages the attention mechanism in Transformer architecture [56] to perform multi-modal fusion in a sequential [2] or a parallel [69] manner. A recent work, ObjectFusion [5], fuses multi-modal features in a two-stage pipeline. It first generates region proposals with the image-augmented BEV features [2], and then extracts the object-centric feature [16, 24] from the voxel, image, and BEV space for further fusion and refinement. In this work, the proposed PoIFusion is also object-centric. However, in contrast to integrating the corresponding region-level feature from multiple modalities, we utilize the PoIs

as the basic units to perform multi-modal fusion, which is adaptively derived from the query box - this element stands as the cornerstone of our approach, fundamentally improving the efficacy and flexibility of our framework.

### 3. Our Approach

In this section, we present the details of our PoIFusion. In Section 3.1, we provide a comprehensive overview of our framework. Then, in Section 3.2, we explain how to generate PoIs based on the object query. Subsequently, in Section 3.3, we introduce the process of multi-modal feature sampling. After that, we elaborate on our dynamic fusion block design in Section 3.4. Finally, in Section 3.5, we detail our prediction head and the training objective.

#### 3.1. Overview

As illustrated in Figure 2, our PoIFusion consists of three main components: (a) an image feature module, (b) a point cloud feature module, and (c) a multi-modal object decoder. Given multi-view images and point clouds, perspective-view image feature maps  $F_I$  and bird-eye-view (BEV) point cloud feature maps  $F_P$  are independently extracted with the camera encoder and the LiDAR encoder. The camera encoder is composed of an image backbone network and an FPN [35] to obtain multi-scale features. The LiDAR encoder exploits the VoxelNet [70, 80] and a BEV backbone network, following the common practice of the voxel-based paradigm. Then, the multi-modal object decoder, which works as the core component in our method, is iteratively applied 6 times, progressively integrating the multi-modal features and refining the detection boxes.

In our multi-modal decoder, each object query  $Q$  is formulated as an adaptive 3D box  $b_t$ , associating with a feature vector  $v_t$  ( $t$  indicates the iteration time step). In each iteration, the object queries are first fed into a self-attention layer to capture the relationships and dependencies between different objects. Here, we follow [38] to exploit a distance-biased self-attention layer in our decoder. Subsequently, for each object query, the box-wise transformation parameters and point-wise shift parameters are generated based on the query feature  $v_t$ , and applied on the query box  $b_t$  to obtain a set of PoIs  $P_t = \{P^i\}$ . To perform multi-modal fusion, a three-step process is undertaken for PoIs. Firstly, each PoI is projected onto both the perspective view and the bird-eye view, establishing the correspondence between the PoI and the multi-modal feature maps. Secondly, the image feature  $f_I$  and point cloud feature  $f_P$  of a PoI are sampled through bilinear interpolation, regarding the projected location on the corresponding view. Thirdly, the extracted multi-modal features at each PoI are dynamically integrated using a dynamic fusion block, followed by a feedforward network (FFN). Finally, a classification head and a regression head are applied to obtain the detection boxes, and the query feature and query box are updated, respectively.

### 3.2. PoI Generation

In this section, we elaborate on how to generate points of interest (PoIs), which serve as the basic units for multi-modal feature fusion in our PoIFusion framework.

Let us consider one object query  $Q = \{b, v\}$  as an example, where  $b$  is the 3D query box and  $v$  is the query feature (the iteration step  $t$  is omitted in the following chapters). The spatial information of  $b$  is presented as  $[x_c, y_c, z_c, w, l, h, \sin\theta, \cos\theta]$ , where  $[x_c, y_c, z_c]$  is the center location,  $[w, l, h]$  is the box dimension, and  $\theta$  is the heading direction in bird-eye view. In the PoI generation block, two sibling linear layers are applied to  $v$ , producing box-wise transformation parameters  $\Delta_B = [t_x, t_y, t_z, t_w, t_l, t_h, t_{\sin}, t_{\cos}]$  and point-wise shift parameters  $\{\Delta_P^i = [\delta_x^i, \delta_y^i, \delta_z^i]\}_{i=0}^8$ . Subsequently, a holistic box transformation according to  $\Delta_B$  is performed on query box  $b$  to obtain transformed box  $b'$ :

$$\begin{aligned} x'_c &= x_c + t_x, & w' &= w \cdot \exp(t_w), \\ y'_c &= y_c + t_y, & l' &= l \cdot \exp(t_l), \\ z'_c &= z_c + t_z, & h' &= h \cdot \exp(t_h), \\ \sin \theta' &= \sin \theta + t_{\sin}, & \cos \theta' &= \cos \theta + t_{\cos}. \end{aligned} \quad (1)$$

Once the box transformation has been applied, the center point and 8 corner points of  $b'$  are collected together as the anchor points  $\{A^i\}_{i=0}^8$ . Finally, the point-wise shift is independently conducted on each anchor point  $A^i$  to produce a PoI  $P^i$  ( $P^i = A^i + \Delta_P^i$ ). It's worth noting that one object query corresponds to a set of PoIs derived from the center and corner points of the query box.

### 3.3. Feature Sampling

In our approach, we assemble multi-modal features by establishing the correspondence between a PoI and multi-modal feature maps via projection, followed by sampling features utilizing bilinear interpolation.

Let us denote the location of a 3D PoI  $P^i$  as  $[x^i, y^i, z^i]$ . To sample the point cloud feature,  $P^i$  is projected onto the bird-eye view (BEV). Since we exploit the voxel representation for point clouds, the location of the projected point on the BEV point cloud feature  $F_P$  is computed as:

$$\begin{cases} m^i = \frac{x^i - X_{\min}}{(X_{\max} - X_{\min}) \times d}, \\ n^i = \frac{y^i - Y_{\min}}{(Y_{\max} - Y_{\min}) \times d}, \end{cases} \quad (2)$$

where  $[m^i, n^i]$  is the projected location,  $[X_{\min}, Y_{\min}, X_{\max}, Y_{\max}]$  is the point cloud range in the BEV, and  $d = 8$  is the downsampling scalar of point cloud feature maps. The point cloud feature sampled at  $[m^i, n^i]$  is denoted as  $f_P^i$ .

Typically, there are multiple surrounding-view cameras on the autonomous vehicle, resulting in multi-view images. A 3D point can be projected onto one or two views. If the PoI is projected to only one view, this view will be leveraged to perform image feature sampling. Otherwise, we follow [5] to randomly choose one view for image feature sampling. Given a 3D PoI  $P^i$  in the LiDAR coordinate system, the projection onto the 2D image plane can be computed as follows:

$$P_{\text{image}}^i = \mathcal{I} \cdot (\mathcal{R} \cdot P^i + \mathcal{T}), \quad (3)$$

where  $P_{\text{image}}^i$  represents the coordinates of the projected PoI on the image plane,  $\mathcal{I}$  is the intrinsic camera matrix,  $\mathcal{R}$  is the rotation matrix of the extrinsic parameters, and  $\mathcal{T}$  is the translation vector of the extrinsic parameters.

In our camera encoder, we exploit an image backbone network followed by an FPN [35] to produce feature maps at P2, P3, P4, and P5 (1/4, 1/8, 1/16, and 1/32 downsampling, respectively). For a given projected point  $P_{\text{image}}^i$ , a set of image feature  $\{g_j^i\}_{j=2}^5$  is sampled from the multi-scale feature maps via bilinear interpolation. The sampled multi-scale image features are then aggregated as:

$$f_I^i = \frac{\sum_{j=2}^5 \exp(w_j^i) \cdot g_j^i}{\sum_{j=2}^5 \exp(w_j^i)}, \quad (4)$$

where  $f_I^i$  represents the aggregated image feature and  $\{w_j^i\}_{j=2}^5$  are scale weight coefficients, which are predicted by a linear layer according to the query feature  $v$ .

### 3.4. Dynamic Multi-Modal Feature Fusion

After feature sampling, each PoI is attached with a multi-modal feature pair. The next step is to fuse the multi-modal

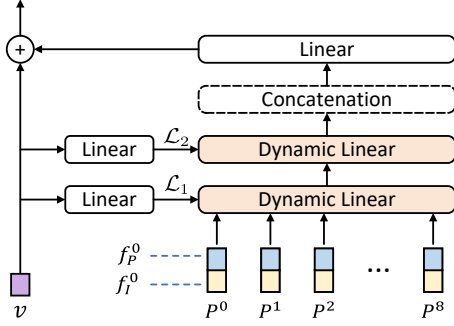


Figure 3. An illustration of our dynamic fusion block.

feature and integrate it into the object query. One simple solution is to exploit a static linear layer over the concatenated feature pair for fusion. However, using static linear layers ignores the fact that the image and point cloud features contribute differently to different objects. To this end, our fusion block capitalizes on a dynamic fusion scheme.

The detail of our dynamic fusion block is depicted in Figure 3. After PoI generation and feature sampling, each object query  $Q$  is represented by a set of PoIs  $\{P^i\}$ , and each PoI is attached with a sampled multi-modal feature pair  $\{f_P^i, f_I^i\}$ . Firstly, we exploit conventional linear layers to produce dynamic fusion parameters  $\mathcal{L}_1$  and  $\mathcal{L}_2$  according to the query feature  $v$ . After that, the concatenated multi-modal feature pair of each PoI is individually integrated through the dynamic linear layers parameterized by  $\mathcal{L}_1$  and  $\mathcal{L}_2$ . Note that the distinction between the dynamic linear layer and the conventional linear layer is that the parameters of the dynamic one are produced on the fly. Subsequently, the features of PoIs derived from the same object query are concatenated together and fed into an additional linear layer to perform PoI feature aggregation. Finally, the aggregated feature is added back to the query feature. The dynamic linear layers and the conventional linear layer leveraged for PoI feature aggregation are followed by a Layer Normalization operation [1] and a ReLU activation layer.

### 3.5. Prediction Head and Training Objective

**Prediction Head.** Our prediction head consists of a classification head and a sibling box regression head. In the classification head, we predict the binary classification score for each category. In the regression head, we follow the iterative refinement scheme [37, 55, 84] to predict the center delta over the predicted box center from the previous iteration. The other parts of the predicted 3D bounding box, including the box dimension, the heading direction, and the velocity, are independently predicted at each time.

**Training Objective.** We follow the practice of set prediction [6] for target assignment. Specifically, we exploit bipartite matching to perform one-to-one assignments between the predicted 3D bounding boxes and the ground-truth boxes. In corresponding to the prediction head, our

training objective also includes two parts: a focal loss [36] for the classification head and an L1 loss for the regression head. The overall training objective is computed as:

$$L = \alpha \cdot L_{cls}(\mathbf{y}_{gt}, \mathbf{y}_{pred}) + \beta \cdot L_{reg}(\mathbf{b}_{gt}, \mathbf{b}_{pred}) \quad (5)$$

where  $\mathbf{y}_{pred}$  is the classification score,  $\mathbf{b}_{pred}$  is the predicted 3D box,  $\alpha$  and  $\beta$  are set as 2.0 and 0.25 following [40, 69] to balance the losses. The training objective is applied to the predicted output of each recurrent iteration.

## 4. Experiments

### 4.1. Experimental Setup

**Dataset and Metric.** We evaluate our method on the nuScenes dataset [4], which includes 700, 150, and 150 driving scenes for training, validation, and testing. The vehicle for data collection is equipped with a 32-beam LiDAR sensor and 6 surrounding-view RGB cameras, thus providing both point clouds and multi-view images. Besides, this dataset annotates more than 1.4 million 3D bounding boxes, across 10 common categories on the street. Both the multi-sensor data and annotation facilitate the exploration of multi-modal 3D object detection. We follow the official policy to mainly evaluate our method in terms of mean average precision (mAP) and nuScenes detection score (NDS). The mAP is averaged over distance thresholds 0.5m, 1m, 2m, and 4m on the BEV across 10 classes. NDS is a weighted average of mAP and other true-positive metrics including mATE, mASE, mAOE, mAVE, and mAAE.

**Network Configuration.** The camera encoder is composed of an image backbone network (*i.e.*, ResNet [23] or Swin-Transformer [41]) and an FPN [35] to enrich the multi-scale information. The LiDAR encoder consists of a 3D sparse VoxelNet [70, 80] and a BEV backbone network. We follow the common practice of setting the image resolution as  $800 \times 448$  and setting the voxel size as (0.075m, 0.075m, 0.2m). In our multi-modal object decoder, there are 900 object queries. The feature dimension of query embedding is set as 256. The channel of image and point cloud features is also transformed to 256 before being fed into the multi-modal decoder. We equally divide the channels of feature maps of each modality into 4 groups, and generate PoIs for each group. This grouping operation improves the capacity of the network [66] and reduces the computation costs of the dynamic fusion block. Moreover, the first dynamic fusion layer halves the channel of the query embedding, and the second dynamic fusion layer restores the feature dimension. The multi-modal object decoder is iteratively applied 6 times, with shared parameters.

**Training and Inference.** We follow the same training pipeline of previous methods [5, 34, 42, 67, 75], and use the same pretrained models. Specifically, the camera encoder is

Method	Present at	Modality	Camera Backbone	LiDAR Backbone	<i>val</i>		<i>test</i>	
					NDS $\uparrow$	mAP $\uparrow$	NDS $\uparrow$	mAP $\uparrow$
DETR3D [63]	CORL'21	C	ResNet-50	-	43.4	34.9	47.9	41.2
BEVFormer [33]	ECCV'22	C	ResNet-50	-	51.7	41.6	56.9	48.1
CenterPoint [76]	CVPR'21	L	-	VoxelNet	66.8	59.6	67.3	60.3
TransFusion-L [2]	CVPR'22	L	-	VoxelNet	70.1	65.1	70.2	65.5
MVP* [77]	NeurIPS'21	C+L	ResNet-50	VoxelNet	70.8	67.1	70.5	66.4
PointAugmenting [58]	CVPR'21	C+L	ResNet-50	VoxelNet	-	-	71.0	66.8
FUTR3D [8]	CVPRW'22	C+L	ResNet-101	VoxelNet	68.3	64.5	-	-
TransFusion [2]	CVPR'22	C+L	ResNet-50	VoxelNet	71.3	67.5	71.6	68.9
UVTR [29]	NeurIPS'22	C+L	ResNet-101	VoxelNet	70.2	65.4	71.1	67.1
BEVFusion (PKU) [34]	NeurIPS'22	C+L	Dual-Swin-T	VoxelNet	72.1	69.6	73.3	71.3
DeepInteraction [75]	NeurIPS'22	C+L	ResNet-50	VoxelNet	72.6	69.9	73.4	70.8
BEVFusion (MIT) [42]	ICRA'23	C+L	Swin-T	VoxelNet	71.4	68.5	72.9	70.2
MSMDFusion* [26]	CVPR'23	C+L	ResNet-50	VoxelNet	72.0	69.3	74.0	71.5
FSF* [31]	arXiv'23	C+L	ResNet-50	Sparse-ResUNet	72.7	70.4	74.0	70.6
UniTR [60]	ICCV'23	C+L	Multi-Modal DSVT	Multi-Modal DSVT	73.1	70.0	74.1	70.5
SparseFusion [67]	ICCV'23	C+L	ResNet-50	VoxelNet	72.8	70.4	73.8	72.0
CMT $\Delta$ [69]	ICCV'23	C+L	VoVNet-99	VoxelNet	72.9	70.3	74.1	72.0
ObjectFusion [5]	ICCV'23	C+L	Swin-T	VoxelNet	72.3	69.8	73.3	71.0
PoIFusion (ours)	-	C+L	ResNet-50	VoxelNet	<b>73.2</b>	<b>71.2</b>	<b>74.3</b>	<b>72.6</b>
PoIFusion (ours)	-	C+L	Swin-T	VoxelNet	<b>73.6</b>	<b>71.7</b>	<b>74.9</b>	<b>73.4</b>

Table 1. **Comparison of 3D object detection performance on nuScenes dataset.** “C” means camera data (RGB images), “L” means LiDAR data (point clouds), “\*” indicates the image input depends on predicted 2D instance masks, and “ $\Delta$ ” indicates the image resolution is enlarged to  $1600 \times 640$ . We highlight the top-2 entries with bold font. We do not apply any test-time augmentation or model ensemble.

initialized with the model weights of a Mask R-CNN [24] model pre-trained on nuImage [4] dataset. The LiDAR encoder is initialized with the model weights of pretrained TransFusion-L [2]. Our fusion framework is trained for 6 epochs with the AdamW optimizer. The training sample is resampled by CBGS [82] strategy. The initial learning rate is set as  $1e-4$ , adapted with the one-cycle learning rate policy, and the weight decay is set as 0.01. To speed up training convergence, the query denoising technique [38, 39, 69] is utilized. Data augmentation including random flip, random rotation, random translation, random scaling, and random modal masking is adopted. We exploit 8 GPUs for training, with 2 samples on each GPU.

At inference, PoIFusion outputs the top 300 detection boxes without NMS. We don’t exploit any test time augmentation or model ensemble techniques.

## 4.2. Comparison with Other Methods

**Main Results of Detection.** In Table 1, we conduct a comprehensive comparison on the nuScenes 3D object detection benchmark. The methods are divided into three groups: camera-based (“C”), LiDAR-based (“L”), and multi-modal (“C+L”). Broadly speaking, the multi-modal methods outperform the methods that leverage only one single modality, validating the benefits of integrating the semantic-intensive RGB image and location-aware LiDAR point clouds.

Our proposed PoIFusion has set a state-of-the-art record on the nuScenes dataset. Specifically, equipped with ResNet-50, our method achieves 73.2% NDS / 71.2% mAP on the validation set and achieves 74.3% NDS / 72.6% mAP on the test set. Upgrading the image backbone to a

Method	Modality	AMOTA (%) $\uparrow$	AMOTP (%) $\downarrow$
CenterPoint [76]	L	63.7	60.6
VoxelNeXt [11]	L	70.2	64.0
TransFusion [2]	C+L	71.8	60.3
BEVFusion (MIT) [42]	C+L	72.8	59.4
ObjectFusion [5]	C+L	74.2	54.3
PoIFusion(ours)	C+L	<b>75.1</b>	<b>50.7</b>

Table 2. **Comparison of 3D multi-object tracking performance.** The results are evaluated on the nuScenes validation set.

Method	mAP	NDS	Latency (ms)	
			A100	V100
Transfusion [2]	67.5	71.3	153.8	190.3
BEVFusion (MIT) [42]	68.5	71.4	<b>113.9</b>	<b>135.5</b>
DeepInteraction [75]	69.9	72.6	204.1	344.8
CMT [69]	70.3	72.9	210.8	387.1
CMT $\dagger$ [69]	70.3	72.9	159.7	-
PoIFusion (ours)	<b>71.2</b>	<b>73.2</b>	115.2	163.7

Table 3. **Runtime comparison.** “ $\dagger$ ” means this model is accelerated with the Flash-Attention Operator [15]. NVIDIA V100 GPU is not compatible with the Flash Attention package.

more powerful Swin-T [41], the performance on the test set boosts to 74.9% NDS and 73.4% mAP, which makes an absolute improvement of 0.8% NDS and 1.4% mAP over the previous best results [69]. Compared to the unified-view methods [29, 34, 42], our PoIFusion better keeps modal-specific information and thus outperforms the representative BEVFusion [42] by 2.0% NDS and 3.2% mAP on the nuScenes test set. In comparison with recent work, *i.e.*, ObjectFusion [5], which also generates object-centric features, our method performs multi-modal fusion at adaptive PoIs, instead of fusing the regional features extracted from different representation spaces. The employment of PoIs



Figure 4. **Qualitative results on the nuScenes validation set.** One example from a sunny day and another example from a rainy night are presented. Our PoIFusion precisely detects 3D objects under varying weather and lighting. We use different colors for different categories.

	NDS	mAP
center only	72.8	70.6
center + corner	<b>73.2</b>	<b>71.2</b>

(a) **Anchor points.** Exploiting both the center and corner points as anchor points for points of interest generation yields better performance.

	NDS	mAP
camera only	40.6	29.4
LiDAR only	70.2	65.3
camera + LiDAR	<b>73.2</b>	<b>71.2</b>

(d) **Ablative experiments of different modalities.** Integrating images and point clouds remarkably boosts the detection result.

	NDS	mAP
baseline	72.4	70.1
+ B.T.	72.8	70.8
+ B.T. & P.S.	<b>73.2</b>	<b>71.2</b>

(b) **Operations to derive PoIs.** Baseline directly uses anchor points, “B.T.” means box transformation, and “P.S.” means point shift.

image resolution	NDS	mAP
800×448	73.2	71.2
1600×640	<b>73.7</b>	<b>71.9</b>

(e) **Image Resolution.** Enlarging the image resolution strengthens the textual information, thus achieving better results.

	NDS	mAP
static fusion	71.8	69.3
dynamic fusion	<b>73.2</b>	<b>71.2</b>

(c) **Fusion block.** Dynamic fusion block produces adaptive parameters for the fusion layer, improving the performance.

voxel size	NDS	mAP
(0.125, 0.125, 0.2)	71.6	69.1
(0.1, 0.1, 0.2)	72.3	69.8
(0.075, 0.075, 0.2)	<b>73.2</b>	<b>71.2</b>

(f) **Voxel size.** Reducing the voxel size leads to a larger resolution of the point cloud feature, benefiting 3D object detection.

Table 4. **Ablative experiments.** In these experiments, the backbone networks are ResNet-50 and VoxelNet. Unless specified, image resolution is set as  $800 \times 448$ , and the voxel size of point clouds is  $(0.075m, 0.075m, 0.2m)$ . Our default setting is highlighted in gray.

improves the flexibility of sampling location and enables fine-grained feature fusion, thus working better. Moreover, the qualitative results are shown in Figure 4, with one example from a sunny day and another example from a rainy night. Our PoIFusion can robustly perform 3D object detection under varying weather and lighting conditions.

**Extended Results of MOT.** In addition to the main results of 3D object detection, we evaluate the generalizability of our method on the 3D multiple object tracking task of the nuScenes dataset. Specifically, we follow CenterPoint [76] to adopt the “tracking-by-detection” scheme that offline links the detection boxes into tracking tubelets. Note that other compared methods, except VoxelNeXt [11], also follow this same scheme. As shown in Table 2, our PoIFusion works the best (75.1% AMOTA and 50.7% AMOTP) among the compared methods, demonstrating our better detection results can also benefit other downstream tasks.

**Runtime Comparison.** Furthermore, we conduct runtime comparisons among the recent works. For a fair comparison, we re-evaluate the latency on an NVIDIA A100 and an

NVIDIA V100 GPU. Since the implementation of the voxelization operation is a confounder for runtime evaluation but will not influence the detection result, we exclude its time cost in comparison. As shown in Table 3, the latency of our PoIFusion is comparable to the fastest method, *i.e.*, BEVFusion (MIT), which further shows the potential of our method to serve as a strong baseline for future investigation.

### 4.3. Ablative Experiments

**Effect of Components in the Multi-Modal Decoder.** In this section, we analyze the design of the proposed multi-modal decoder from three aspects: (a) anchor points, (b) operations to generate PoIs, and (c) the fusion block. As shown in Table 4a, the model that only uses the center point achieves 72.8% NDS and 70.6% mAP. By additionally involving the corner points, the NDS and mAP boosts to 73.2% and 71.2%, respectively. This comparison shows the benefits of representing the geometric property of query boxes. In Table 4b, we validate the operations to derive PoIs from anchor points. The baseline directly takes the anchor

Offsets (m)	0.0	0.2	0.4	0.6	0.8	1.0
NDS (%)	73.2	73.0	72.9	72.7	72.3	72.0
mAP (%)	71.2	71.1	70.8	70.5	70.0	69.4

Table 5. **Sensor misalignment.** Performance comparison on the impact of translation offsets due to calibration errors.

points as PoIs without adaptation, achieving 70.1% mAP. By involving the holistic box-level transformation and further applying the point-wise shift, the performance boosts to 70.8 % mAP and 71.2% mAP, respectively. The online adjustment of PoIs ameliorates the misalignment in feature sampling and thereby boosts the detection result.

Table 4c compares the effect of different fusion schemes, *i.e.*, static fusion versus dynamic fusion. In static fusion, two conventional linear layers are exploited to process the concatenated multi-modal features at each PoI. The dynamic fusion scheme refers to our proposed one in Section 3.4. Thanks to the adjustment of fusion layers’ parameters for each individual object query, our dynamic fusion outperforms the static setting by 1.4% NDS and 1.9% mAP.

**Effect of Different Modalities.** In this experiment, we train models with single-modality input following the same setting as our default one. As shown in Table 4d, the image-only baseline achieves 40.6% NDS and 29.4% mAP. Meanwhile, the LiDAR-only baseline achieves 70.2% NDS and 65.3% mAP, which is similar to TransFusion-L [2] (70.1% NDS and 65.1% mAP). Integrating the multi-modal information remarkably boosts the performance to 73.2% NDS and 71.2% mAP, validating the capability of our proposed fusion paradigm to integrate the complementary information from images and point clouds.

**Effect of the Input Resolution.** The input resolution is also one of the key factors that influence the detection result. In Table 4e, we enlarge the image resolution from  $800 \times 448$  to  $1600 \times 640$ , obtaining 0.5% NDS and 0.7% mAP gain. In Table 4f, we further analyze the influence of the voxel size. Either a larger image resolution or a smaller voxel size facilitates the feature representation of the corresponding modality, thus boosting the detection result. Our default setting employs an image resolution of  $800 \times 448$  and a voxel size of  $(0.0075m, 0.0075m, 0.2m)$ , which is the same as most of recent works [2, 5, 67, 75].

#### 4.4. Detection Robustness Analysis

**Sensor Misalignment.** In real applications, sensors can be misaligned due to physical impacts, installation errors, time-related drift, or some other unexpected reasons. This experiment investigates the robustness of PoIFusion against sensor misalignment. Specifically, we follow [2] to randomly add translation offsets to the calibration matrix at inference. The errors are formulated as uniformly distributed noise, with the maximum offset value varying from  $0.2m$  to  $1.0m$ . As shown in Table 5, even when the maximum

# Dropped Images	0	1	3	6
NDS (%)	73.2	72.8	72.0	70.2
mAP (%)	71.2	70.3	68.6	65.6

Table 6. **Camera failure.** Performance comparison on the impact of dropped images due to camera failure.

Discarded Sectors	0°	6°	12°	18°	24°
NDS (%)	73.2	72.7	72.0	71.3	70.7
mAP (%)	71.2	70.2	68.9	67.6	66.4

Table 7. **LiDAR failure.** Performance comparison on the impact of discarded point clouds within a sector due to LiDAR failure.

translation offset is  $1.0m$ , our method can achieve 72.0% NDS and 69.4% mAP, demonstrating the robustness of our fusion paradigm against sensor misalignment.

**Sensor Failure.** In addition to sensor misalignment, we further explore a more serious condition, *i.e.*, sensor failure. To validate our method under camera failure cases, we randomly drop several images by filling the corresponding images as all zeros. The results with different numbers of dropped images are presented in Table 6. The performance keeps dropping along with the increasing number of cameras that fail to work. Even with half of the cameras blocked, our PoIFusion achieves 68.6% mAP, obviously better than the LiDAR-only method. Moreover, in the extreme case that all of the cameras are not working, our method works comparable to the LiDAR-only baseline.

Furthermore, to simulate the failure of a LiDAR sensor, we randomly discard point cloud data within a specified sectorial region based on the azimuthal angle. As shown in Table 7, in general, the impact of LiDAR failure is more pronounced than that of camera failure, since the spatial information captured by the LiDAR sensor is essential for precise localization. Notwithstanding the total absence of point cloud data within a  $24^\circ$  sector, the mAP achieved by our method is still 1.1% higher than the LiDAR-only baseline. These two experiments demonstrate the robustness of our proposed PoIFusion against Sensor Failure.

## 5. Conclusion

In this work, we present PoIFusion, a query-based multi-modal 3D object detector, which is characterized by performing multi-modal feature sampling and fusion at generated points of interest. On the one hand, PoIFusion keeps the original view of the image and point cloud feature to preserve the modal-specific information. On the other hand, the employment of points of interest facilitates fine-grained fusion and enables representing object features in a flexible way. Our PoIFusion sets a state-of-the-art record on the highly competitive nuScenes dataset, and in the meantime keeps efficient runtime. Moreover, the experimental analysis demonstrates our method is robust to sensor misalignment and failure. We suppose our PoIFusion would serve as a strong baseline with huge potential for future exploration.



## References

- [1] Jimmy Lei Ba, Jamie Ryan Kiros, and Geoffrey E Hinton. Layer normalization. *arXiv preprint arXiv:1607.06450*, 2016. 5
- [2] Xuyang Bai, Zeyu Hu, Xinge Zhu, Qingqiu Huang, Yilun Chen, Hongbo Fu, and Chiew-Lan Tai. Transfusion: Robust lidar-camera fusion for 3d object detection with transformers. In *Proceedings of the IEEE/CVF Conference on Computer Vision and Pattern Recognition (CVPR)*, 2022. 1, 3, 6, 8, 2
- [3] Garrick Brazil and Xiaoming Liu. M3d-rpn: Monocular 3d region proposal network for object detection. In *Proceedings of the IEEE/CVF International Conference on Computer Vision (ICCV)*, 2019. 2
- [4] Holger Caesar, Varun Bankiti, Alex H Lang, Sourabh Vora, Venice Erin Liong, Qiang Xu, Anush Krishnan, Yu Pan, Giancarlo Baldan, and Oscar Beijbom. nuScenes: A multi-modal dataset for autonomous driving. In *Proceedings of the IEEE/CVF Conference on Computer Vision and Pattern Recognition (CVPR)*, 2020. 5, 6
- [5] Qi Cai, Yingwei Pan, Ting Yao, Chong-Wah Ngo, and Tao Mei. Objectfusion: Multi-modal 3d object detection with object-centric fusion. In *Proceedings of the IEEE/CVF International Conference on Computer Vision (ICCV)*, 2023. 2, 3, 4, 5, 6, 8
- [6] Nicolas Carion, Francisco Massa, Gabriel Synnaeve, Nicolas Usunier, Alexander Kirillov, and Sergey Zagoruyko. End-to-end object detection with transformers. In *Proceedings of the European Conference on Computer Vision (ECCV)*, 2020. 1, 3, 5
- [7] Xiaozhi Chen, Huimin Ma, Ji Wan, Bo Li, and Tian Xia. Multi-View 3D Object Detection Network for Autonomous Driving. In *Proceedings of the IEEE/CVF Conference on Computer Vision and Pattern Recognition (CVPR)*, 2017. 3
- [8] Xuanyao Chen, Tianyuan Zhang, Yue Wang, Yilun Wang, and Hang Zhao. FUTR3D: A unified sensor fusion framework for 3d detection. *arXiv preprint arXiv:2203.10642*, 2022. 2, 3, 6
- [9] Yukang Chen, Yanwei Li, Xiangyu Zhang, Jian Sun, and Jiaya Jia. Focal Sparse Convolutional Networks for 3D Object Detection. In *Proceedings of the IEEE/CVF Conference on Computer Vision and Pattern Recognition (CVPR)*, 2022. 2
- [10] Yukang Chen, Jianhui Liu, Xiaojuan Qi, Xiangyu Zhang, Jian Sun, and Jiaya Jia. Scaling up kernels in 3D CNNs. *arXiv preprint arXiv:2206.10555*, 2022. 2
- [11] Yukang Chen, Jianhui Liu, Xiangyu Zhang, Xiaojuan Qi, and Jiaya Jia. VoxelNeXt: Fully Sparse VoxelNet for 3D Object Detection and Tracking. In *Proceedings of the IEEE/CVF Conference on Computer Vision and Pattern Recognition (CVPR)*, 2023. 6, 7
- [12] Yilun Chen, Zhiding Yu, Yukang Chen, Shiyi Lan, Anima Anandkumar, Jiaya Jia, and Jose M Alvarez. Focalformer3d: Focusing on hard instance for 3d object detection. In *Proceedings of the IEEE/CVF International Conference on Computer Vision (ICCV)*, 2023. 2
- [13] Zehui Chen, Zhenyu Li, Shiquan Zhang, Liangji Fang, Qinghong Jiang, Feng Zhao, Bolei Zhou, and Hang Zhao. Autoalign: Pixel-instance feature aggregation for multi-modal 3d object detection. *Proceedings of the European Conference on Computer Vision (ECCV)*, 2022. 3
- [14] Zhiyu Chong, Xinzhu Ma, Hong Zhang, Yuxin Yue, Haojie Li, Zihui Wang, and Wanli Ouyang. Monodistill: Learning spatial features for monocular 3d object detection. *arXiv preprint arXiv:2201.10830*, 2022. 2
- [15] Tri Dao, Dan Fu, Stefano Ermon, Atri Rudra, and Christopher Ré. Flashattention: Fast and memory-efficient exact attention with io-awareness. In *Proceedings of the Advances in Neural Information Processing Systems (NeurIPS)*, 2022. 2, 6
- [16] Jiajun Deng, Shaoshuai Shi, Peiwei Li, Wengang Zhou, Yanyong Zhang, and Houqiang Li. Voxel R-CNN: Towards High Performance Voxel-based 3D Object Detection. In *Proceedings of the AAAI Conference on Artificial Intelligence (AAAI)*, 2021. 2, 3
- [17] Jiajun Deng, Wengang Zhou, Yanyong Zhang, and Houqiang Li. From multi-view to hollow-3d: Hallucinated hollow-3d r-cnn for 3d object detection. *IEEE Transactions on Circuits and Systems for Video Technology (TCSVT)*, 2021. 2
- [18] Shaocong Dong, Lihe Ding, Haiyang Wang, Tingfa Xu, Xinli Xu, Jie Wang, Ziyang Bian, Ying Wang, and Jianan Li. Mssvt: Mixed-scale sparse voxel transformer for 3d object detection on point clouds. *Proceedings of the Advances in Neural Information Processing Systems (NeurIPS)*, 2022. 2
- [19] Lue Fan, Ziqi Pang, Tianyuan Zhang, Yu-Xiong Wang, Hang Zhao, Feng Wang, Naiyan Wang, and Zhaoxiang Zhang. Embracing Single Stride 3D Object Detector with Sparse Transformer. In *Proceedings of the IEEE/CVF Conference on Computer Vision and Pattern Recognition (CVPR)*, 2022. 2
- [20] Lue Fan, Feng Wang, Naiyan Wang, and Zhaoxiang Zhang. Fully Sparse 3D Object Detection. In *Proceedings of the Advances in Neural Information Processing Systems (NeurIPS)*, 2022. 2
- [21] Ziteng Gao, Limin Wang, Bing Han, and Sheng Guo. Adamixer: A fast-converging query-based object detector. In *Proceedings of the IEEE/CVF Conference on Computer Vision and Pattern Recognition (CVPR)*, 2022. 2
- [22] Chongjian Ge, Junsong Chen, Enze Xie, Zhongdao Wang, Lanqing Hong, Huchuan Lu, Zhenguo Li, and Ping Luo. Metabev: Solving sensor failures for 3d detection and map segmentation. In *Proceedings of the IEEE/CVF International Conference on Computer Vision (ICCV)*, 2023. 1, 3
- [23] Kaiming He, Xiangyu Zhang, Shaoqing Ren, and Jian Sun. Deep Residual Learning for Image Recognition. In *Proceedings of the IEEE/CVF Conference on Computer Vision and Pattern Recognition (CVPR)*, 2016. 5
- [24] Kaiming He, Georgia Gkioxari, Piotr Dollár, and Ross Girshick. Mask R-CNN. In *Proceedings of the IEEE/CVF International Conference on Computer Vision (ICCV)*, 2017. 3, 6
- [25] Junjie Huang, Guan Huang, Zheng Zhu, Yun Ye, and Dalong Du. Bevdet: High-performance multi-camera 3d object de-

- tection in bird-eye-view. *arXiv preprint arXiv:2112.11790*, 2021. 2
- [26] Yang Jiao, Zequn Jie, Shaoxiang Chen, Jingjing Chen, Lin Ma, and Yu-Gang Jiang. Msmdfusion: Fusing lidar and camera at multiple scales with multi-depth seeds for 3d object detection. In *Proceedings of the IEEE/CVF Conference on Computer Vision and Pattern Recognition (CVPR)*, 2023. 3, 6
- [27] Xin Lai, Yukang Chen, Fanbin Lu, Jianhui Liu, and Jiaya Jia. Spherical transformer for lidar-based 3d recognition. In *Proceedings of the IEEE/CVF Conference on Computer Vision and Pattern Recognition (CVPR)*, 2023. 2
- [28] Alex H Lang, Sourabh Vora, Holger Caesar, Lubing Zhou, Jiong Yang, and Oscar Beijbom. PointPillars: Fast Encoders for Object Detection from Point Clouds. In *Proceedings of the IEEE/CVF Conference on Computer Vision and Pattern Recognition (CVPR)*, 2019. 2
- [29] Yanwei Li, Yilun Chen, Xiaojuan Qi, Zeming Li, Jian Sun, and Jiaya Jia. Unifying voxel-based representation with transformer for 3d object detection. In *Proceedings of the Advances in Neural Information Processing Systems (NeurIPS)*, 2022. 1, 3, 6
- [30] Yingwei Li, Adams Wei Yu, Tianjian Meng, Ben Caine, Jiquan Ngiam, Daiyi Peng, Junyang Shen, Bo Wu, Yifeng Lu, Denny Zhou, et al. DeepFusion: Lidar-Camera Deep Fusion for Multi-Modal 3D Object Detection. In *Proceedings of the IEEE/CVF Conference on Computer Vision and Pattern Recognition (CVPR)*, 2022. 3
- [31] Yingyan Li, Lue Fan, Yang Liu, Zehao Huang, Yuntao Chen, Naiyan Wang, Zhaoxiang Zhang, and Tieniu Tan. Fully sparse fusion for 3d object detection. *arXiv preprint arXiv:2304.12310*, 2023. 3, 6
- [32] Yinhao Li, Zheng Ge, Guanyi Yu, Jinrong Yang, Zengran Wang, Yukang Shi, Jianjian Sun, and Zeming Li. BevDepth: Acquisition of reliable depth for multi-view 3d object detection. In *Proceedings of the AAAI Conference on Artificial Intelligence (AAAI)*, 2023. 2
- [33] Zhiqi Li, Wenhai Wang, Hongyang Li, Enze Xie, Chonghao Sima, Tong Lu, Yu Qiao, and Jifeng Dai. BevFormer: Learning bird’s-eye-view representation from multi-camera images via spatiotemporal transformers. In *Proceeding of the 16th European Conference on Computer Vision (ECCV)*, 2022. 2, 6
- [34] Tingting Liang, Hongwei Xie, Kaicheng Yu, Zhongyu Xia, Zhiwei Lin, Yongtao Wang, Tao Tang, Bing Wang, and Zhi Tang. BEVFusion: A simple and robust lidar-camera fusion framework. In *Proceedings of the Advances in Neural Information Processing Systems (NeurIPS)*, 2022. 1, 3, 5, 6
- [35] Tsung-Yi Lin, Piotr Dollár, Ross Girshick, Kaiming He, Bharath Hariharan, and Serge Belongie. Feature Pyramid Networks for Object Detection. In *Proceedings of the IEEE/CVF Conference on Computer Vision and Pattern Recognition (CVPR)*, 2017. 3, 4, 5
- [36] Tsung-Yi Lin, Priya Goyal, Ross Girshick, Kaiming He, and Piotr Dollár. Focal Loss for Dense Object Detection. In *Proceedings of the IEEE/CVF International Conference on Computer Vision (ICCV)*, 2017. 5
- [37] Yutong Lin, Yuhui Yuan, Zheng Zhang, Chen Li, Nanning Zheng, and Han Hu. Detr does not need multi-scale or locality design. In *Proceedings of the IEEE/CVF International Conference on Computer Vision (ICCV)*, 2023. 5
- [38] Haisong Liu, Yao Teng, Tao Lu, Haiguang Wang, and Limin Wang. Sparsebev: High-performance sparse 3d object detection from multi-camera videos. In *Proceedings of the IEEE/CVF International Conference on Computer Vision (ICCV)*, 2023. 3, 4, 6, 1
- [39] Shilong Liu, Feng Li, Hao Zhang, Xiao Yang, Xianbiao Qi, Hang Su, Jun Zhu, and Lei Zhang. Dab-detr: Dynamic anchor boxes are better queries for detr. In *International Conference on Learning Representations (ICLR)*, 2022. 6
- [40] Yingfei Liu, Tiancai Wang, Xiangyu Zhang, and Jian Sun. PETR: Position embedding transformation for multi-view 3d object detection. In *Proceeding of the 16th European Conference on Computer Vision (ECCV)*, 2022. 1, 2, 3, 5
- [41] Ze Liu, Yutong Lin, Yue Cao, Han Hu, Yixuan Wei, Zheng Zhang, Stephen Lin, and Baining Guo. Swin Transformer: Hierarchical Vision Transformer Using Shifted Windows. In *Proceedings of the IEEE/CVF International Conference on Computer Vision (ICCV)*, 2021. 5, 6
- [42] Zhijian Liu, Haotian Tang, Alexander Amini, Xinyu Yang, Huizi Mao, Daniela Rus, and Song Han. BEVFusion: Multi-Task Multi-Sensor Fusion with Unified Bird’s-Eye View Representation. In *Proceeding of the IEEE International Conference on Robotics and Automation (ICRA)*, 2023. 1, 3, 5, 6, 2
- [43] Yan Lu, Xinzhu Ma, Lei Yang, Tianzhu Zhang, Yating Liu, Qi Chu, Junjie Yan, and Wanli Ouyang. Geometry uncertainty projection network for monocular 3d object detection. In *Proceedings of the IEEE/CVF International Conference on Computer Vision (ICCV)*, 2021. 2
- [44] Jiageng Mao, Yujing Xue, Minzhe Niu, Haoyue Bai, Jiashi Feng, Xiaodan Liang, Hang Xu, and Chunjing Xu. Voxel transformer for 3d object detection. In *Proceedings of the IEEE/CVF International Conference on Computer Vision (ICCV)*, 2021. 2
- [45] Jonah Philion and Sanja Fidler. Lift, Splat, Shoot: Encoding images from arbitrary camera rigs by implicitly unprojecting to 3D. In *Proceeding of the 16th European Conference on Computer Vision (ECCV)*, 2020. 3
- [46] Charles R Qi, Hao Su, Kaichun Mo, and Leonidas J Guibas. PointNet: Deep Learning on Point Sets for 3D Classification and Segmentation. In *Proceedings of the IEEE/CVF Conference on Computer Vision and Pattern Recognition (CVPR)*, 2017. 2
- [47] Charles Ruizhongtai Qi, Li Yi, Hao Su, and Leonidas J Guibas. PointNet++: Deep Hierarchical Feature Learning on Point Sets in a Metric Space. In *Proceedings of the Advances in Neural Information Processing Systems (NeurIPS)*, 2017. 2
- [48] Cody Reading, Ali Harakeh, Julia Chae, and Steven L Waslander. Categorical depth distribution network for monocular 3D object detection. In *Proceedings of the IEEE/CVF Conference on Computer Vision and Pattern Recognition (CVPR)*, 2021. 2

- [49] Hualian Sheng, Sijia Cai, Yuan Liu, Bing Deng, Jianqiang Huang, Xian-Sheng Hua, and Min-Jian Zhao. Improving 3d object detection with channel-wise transformer. In *Proceedings of the IEEE/CVF International Conference on Computer Vision (ICCV)*, 2021. 2
- [50] Guangsheng Shi, Ruifeng Li, and Chao Ma. PillarNet: High-Performance Pillar-based 3D Object Detection. *arXiv preprint arXiv:2205.07403*, 2022. 2
- [51] Shaoshuai Shi, Xiaogang Wang, and Hongsheng Li. PointRCNN: 3D Object Proposal Generation and Detection from Point Cloud. In *Proceedings of the IEEE/CVF Conference on Computer Vision and Pattern Recognition (CVPR)*, 2019. 2
- [52] Shaoshuai Shi, Chaoxu Guo, Li Jiang, Zhe Wang, Jianping Shi, Xiaogang Wang, and Hongsheng Li. PV-RCNN: Point-Voxel Feature Set Abstraction for 3D Object Detection. In *Proceedings of the IEEE/CVF Conference on Computer Vision and Pattern Recognition (CVPR)*, 2020. 2
- [53] Shaoshuai Shi, Li Jiang, Jiajun Deng, Zhe Wang, Chaoxu Guo, Jianping Shi, Xiaogang Wang, and Hongsheng Li. PV-RCNN+: Point-Voxel Feature Set Abstraction With Local Vector Representation for 3D Object Detection. *arXiv preprint arXiv:2102.00463*, 2021. 2
- [54] Changyong Shu, Jiajun Deng, Fisher Yu, and Yifan Liu. 3dppe: 3d point positional encoding for transformer-based multi-camera 3d object detection. In *Proceedings of the IEEE/CVF International Conference on Computer Vision (ICCV)*, 2023. 3
- [55] Zachary Teed and Jia Deng. Raft: Recurrent all-pairs field transforms for optical flow. In *Proceeding of the 16th European Conference on Computer Vision (ECCV)*, 2020. 5
- [56] Ashish Vaswani, Noam Shazeer, Niki Parmar, Jakob Uszkoreit, Llion Jones, Aidan N Gomez, Łukasz Kaiser, and Illia Polosukhin. Attention Is All You Need. In *Proceedings of the Advances in Neural Information Processing Systems (NeurIPS)*, 2017. 1, 3
- [57] Sourabh Vora, Alex H Lang, Bassam Helou, and Oscar Beijbom. PointPainting: Sequential Fusion for 3D Object Detection. In *Proceedings of the IEEE/CVF Conference on Computer Vision and Pattern Recognition (CVPR)*, 2020. 3
- [58] Chunwei Wang, Chao Ma, Ming Zhu, and Xiaokang Yang. PointAugmenting: Cross-modal augmentation for 3d object detection. In *Proceedings of the IEEE/CVF Conference on Computer Vision and Pattern Recognition (CVPR)*, 2021. 3, 6
- [59] Haiyang Wang, Chen Shi, Shaoshuai Shi, Meng Lei, Sen Wang, Di He, Bernt Schiele, and Liwei Wang. Dsvt: Dynamic sparse voxel transformer with rotated sets. In *Proceedings of the IEEE/CVF Conference on Computer Vision and Pattern Recognition (CVPR)*, 2023. 2
- [60] Haiyang Wang, Hao Tang, Shaoshuai Shi, Aoxue Li, Zhenguo Li, Bernt Schiele, and Liwei Wang. Unitr: A unified and efficient multi-modal transformer for bird's-eye-view representation. In *Proceedings of the IEEE/CVF International Conference on Computer Vision (ICCV)*, 2023. 3, 6
- [61] Tai Wang, Xinge Zhu, Jiangmiao Pang, and Dahua Lin. Fcos3d: Fully convolutional one-stage monocular 3D object detection. In *Proceedings of the IEEE/CVF Conference on Computer Vision and Pattern Recognition (CVPR)*, 2021. 2
- [62] Yan Wang, Wei-Lun Chao, Divyansh Garg, Bharath Hariharan, Mark Campbell, and Kilian Q Weinberger. Pseudolidar from visual depth estimation: Bridging the gap in 3d object detection for autonomous driving. In *Proceedings of the IEEE/CVF Conference on Computer Vision and Pattern Recognition (CVPR)*, 2019. 2
- [63] Yue Wang, Vitor Campagnolo Guizilini, Tianyuan Zhang, Yilun Wang, Hang Zhao, and Justin Solomon. DETR3D: 3D object detection from multi-view images via 3d-to-2d queries. In *Proceedings of the Conference on Robot Learning (CoRL)*, 2022. 3, 6
- [64] Yingjie Wang, Qiuyu Mao, Hanqi Zhu, Jiajun Deng, Yu Zhang, Jianmin Ji, Houqiang Li, and Yanyong Zhang. Multi-modal 3d object detection in autonomous driving: a survey. *International Journal of Computer Vision (IJCV)*, 2023. 1
- [65] Zitian Wang, Zehao Huang, Jiahui Fu, Naiyan Wang, and Si Liu. Object as query: Lifting any 2d object detector to 3d detection. In *Proceedings of the IEEE/CVF International Conference on Computer Vision (ICCV)*, 2023. 3
- [66] Saining Xie, Ross Girshick, Piotr Dollár, Zhuowen Tu, and Kaiming He. Aggregated residual transformations for deep neural networks. In *Proceedings of the IEEE conference on computer vision and pattern recognition (CVPR)*, 2017. 5
- [67] Yichen Xie, Chenfeng Xu, Marie-Julie Rakotosaona, Patrick Rim, Federico Tombari, Kurt Keutzer, Masayoshi Tomizuka, and Wei Zhan. Sparsefusion: Fusing multi-modal sparse representations for multi-sensor 3d object detection. In *Proceedings of the IEEE/CVF International Conference on Computer Vision (ICCV)*, 2023. 3, 5, 6, 8, 2
- [68] Kaixin Xiong, Shi Gong, Xiaoqing Ye, Xiao Tan, Ji Wan, Errui Ding, Jingdong Wang, and Xiang Bai. Cape: Camera view position embedding for multi-view 3d object detection. In *Proceedings of the IEEE/CVF Conference on Computer Vision and Pattern Recognition (CVPR)*, 2023. 3
- [69] Junjie Yan, Yingfei Liu, Jianjian Sun, Fan Jia, Shuailin Li, Tiancai Wang, and Xiangyu Zhang. Cross modal transformer: Towards fast and robust 3d object detection. In *Proceedings of the IEEE/CVF International Conference on Computer Vision (ICCV)*, 2023. 1, 2, 3, 5, 6
- [70] Yan Yan, Yuxing Mao, and Bo Li. SECOND: Sparsely Embedded Convolutional Detection. *Sensors*, 18(10), 2018. 2, 3, 5
- [71] Chenyu Yang, Yuntao Chen, Hao Tian, Chenxin Tao, Xizhou Zhu, Zhaoxiang Zhang, Gao Huang, Hongyang Li, Yu Qiao, et al. Bevformer v2: Adapting modern image backbones to bird's-eye-view recognition via perspective supervision. In *Proceedings of the IEEE/CVF Conference on Computer Vision and Pattern Recognition (CVPR)*, 2023. 2
- [72] Jihan Yang, Shaoshuai Shi, Runyu Ding, Zhe Wang, and Xiaojuan Qi. Towards efficient 3d object detection with knowledge distillation. *Advances in Neural Information Processing Systems (NeurIPS)*, 2022. 2
- [73] Zetong Yang, Yanan Sun, Shu Liu, Xiaoyong Shen, and Jiaya Jia. STD: Sparse-to-Dense 3D Object Detector for Point Cloud. In *Proceedings of the IEEE/CVF International Conference on Computer Vision (ICCV)*, 2019. 2

- [74] Zetong Yang, Yanan Sun, Shu Liu, and Jiaya Jia. 3DSSD: Point-based 3D Single Stage Object Detector. In *Proceedings of the IEEE/CVF Conference on Computer Vision and Pattern Recognition (CVPR)*, 2020. 2
- [75] Zeyu Yang, Jiaqi Chen, Zhenwei Miao, Wei Li, Xiatian Zhu, and Li Zhang. DeepInteraction: 3D object detection via modality interaction. In *Proceedings of the Advances in Neural Information Processing Systems (NeurIPS)*, 2022. 1, 3, 5, 6, 8, 2
- [76] Tianwei Yin, Xingyi Zhou, and Philipp Krähenbühl. Center-based 3D Object Detection and Tracking. In *Proceedings of the IEEE/CVF Conference on Computer Vision and Pattern Recognition (CVPR)*, 2021. 2, 6, 7
- [77] Tianwei Yin, Xingyi Zhou, and Philipp Krähenbühl. Multi-modal virtual point 3d detection. In *Proceedings of the Advances in Neural Information Processing Systems (NeurIPS)*, 2021. 3, 6
- [78] Jin Hyeok Yoo, Yecheol Kim, Jisong Kim, and Jun Won Choi. 3D-CVF: Generating joint camera and lidar features using cross-view spatial feature fusion for 3d object detection. In *Proceeding of the 16th European Conference on Computer Vision (ECCV)*, 2020. 3
- [79] Renrui Zhang, Han Qiu, Tai Wang, Ziyu Guo, Ziteng Cui, Yu Qiao, Hongsheng Li, and Peng Gao. Monodetr: Depth-guided transformer for monocular 3d object detection. In *Proceedings of the IEEE/CVF International Conference on Computer Vision (ICCV)*, 2023. 2
- [80] Yin Zhou and Oncel Tuzel. VoxelNet: End-to-End Learning for Point Cloud Based 3D Object Detection. In *Proceedings of the IEEE/CVF Conference on Computer Vision and Pattern Recognition (CVPR)*, 2018. 2, 3, 5
- [81] Zixiang Zhou, Xiangchen Zhao, Yu Wang, Panqu Wang, and Hassan Foroosh. CenterFormer: Center-based Transformer for 3D Object Detection. In *Proceeding of the 16th European Conference on Computer Vision (ECCV)*, 2022. 2
- [82] Benjin Zhu, Zhengkai Jiang, Xiangxin Zhou, Zeming Li, and Gang Yu. Class-balanced grouping and sampling for point cloud 3d object detection. *arXiv preprint arXiv:1908.09492*, 2019. 6
- [83] Hanqi Zhu, Jiajun Deng, Yu Zhang, Jianmin Ji, Qiuyu Mao, Houqiang Li, and Yanyong Zhang. Vpfnet: Improving 3d object detection with virtual point based lidar and stereo data fusion. *IEEE Transactions on Multimedia*, 2022. 3
- [84] Xizhou Zhu, Weijie Su, Lewei Lu, Bin Li, Xiaogang Wang, and Jifeng Dai. Deformable DETR: Deformable Transformers for End-to-End Object Detection. In *Proceedings of the IEEE International Conference on Robotics and Automation (ICLR)*, 2020. 2, 5

# PoIFusion: Multi-Modal 3D Object Detection via Fusion at Points of Interest

## Supplementary Material

This supplementary material is composed of three sections. In Section A, we introduce supplementary details of our implementation. Then, in Section B, we provide additional experiments to further validate the merits of our proposed method. Finally, in section C, we visualize more examples to help intuitively present the detection results.

### A. Supplementary Details

**Query Initialization.** As introduced in our main paper, we formulate each object query as a learnable dynamic 3D box  $\mathbf{b} \in \mathbb{R}^8$  and an attached feature vector  $\mathbf{v} \in \mathbb{R}^{256}$ . Specifically, the query box is represented as:

$$\mathbf{b} = [x_c, y_c, z_c, w, l, h, \sin\theta, \cos\theta], \quad (6)$$

where  $[x_c, y_c, z_c]$  is the center location,  $[w, l, h]$  is the box dimension, and  $\theta$  is the azimuth angle. Notably, while velocity is a component of the detection results, it is not factored into the query boxes. When we initialize the query box, the BEV center location  $[x_c, y_c]$  is set to be uniformly distributed on the BEV, and the height center  $z_c$  is set as 0. Besides, the dimensions  $w, l, h$  of each box are respectively initialized as 6, 3, 2, and the azimuth is initialized as 0.

**Distance-Biased Self-Attention Layer.** As outlined in Section 3.1, the multi-modal decoder utilizes a distance-biased self-attention layer [38] to capture the relationships and dependencies between different object queries. Here, we provide a comprehensive review of it.

Specifically, a conventional self-attention layer [56] calculates the attention score based on the dot product of query and key, which is detailed as:

$$\text{Attn\_Score}(Q, K) = \text{Softmax}\left(\frac{QK^T}{\sqrt{C}}\right), \quad (7)$$

where Q and K correspond to the query and key, and C is the channel dimension. The distance-biased self-attention layer incorporates a bias term that is contingent upon the centroid distance between pairs of query boxes. The adjusted attention score is computed as:

$$\text{Attn\_Score}(Q, K, D) = \text{Softmax}\left(\frac{QK^T}{\sqrt{C}} - \psi \cdot D\right), \quad (8)$$

where  $D$  indicates the centroid distance between query boxes, and  $\psi$  is a scalar produced by a linear layer according to the query feature. In our multi-modal object decoder, we use 8 heads in the self-attention layer. The  $\psi$  is not shared in different heads. We emphasize that the distance-biased self-attention layer is not the contribution of our work. We implement the self-attention layer with it since it improves the adaptability of the model with negligible costs.

### B. Additional Experimental Analysis

**Different Weathers and Lighting Conditions.** The 3D object detection system on autonomous driving vehicles is supposed to be capable of working under varying lighting and weather conditions. In the main manuscript, we have shown two qualitative examples to give a glimpse of the robustness of our PoIFusion. In this experiment, we further follow [42] to divide the validation set of the nuScenes dataset into two pairs of subsets: sunny/rainy and day/night for comprehensive quantitative evaluation. The evaluated performance in terms of mAP (%) is summarized in Table S1. In general, the multi-modal 3D object detectors are not likely to be affected by the rainy weather. The changing of lighting condition significantly affects the detection performance, *i.e.*, the mAP on the night subset is much lower than that of the day subset. Among the compared methods, our PoIFusion achieves the best performance under different weather and lighting conditions, further demonstrating the robustness of our fusion strategy.

mAP (%)	Modality	Sunny	Rainy	Day	Night
BEVDet	C	32.9	33.7	33.7	13.5
Centerpoint	L	62.9	59.2	62.8	35.4
MVP	C+L	65.9	66.3	66.3	38.4
BEVFusion	C+L	68.2	69.9	68.5	42.8
PoIFusion (ours)	C+L	<b>71.1</b>	<b>70.2</b>	<b>71.3</b>	<b>45.0</b>

Table S1. **Different lighting and weather conditions.** The reported performance is compared in terms of mAP (%) on the nuScenes validation set. We report the result of our PoIFusion with the Swin-T image backbone network.

#### Effect of Iteration Times of the Multi-Modal Decoder.

As introduced in Section 3.1, our multi-modal object decoder is iteratively applied to perform feature fusion and box refinement. In Table S2, we analyze how the iteration times of our multi-modal decoder influence the 3D object detection performance. Specifically, we vary the iteration times from 1 to 8 times and re-train the model for evaluation. In the beginning, the performance consistently improves along with the increasing iteration time. The peak performance is achieved when we apply the multi-modal object decoder 6 times. When we further increase the iteration time to 8, the performance drops for 0.5% NDS and 0.9% mAP. Therefore, in our default configuration, the multi-modal object decoder is iteratively applied 6 times. Moreover, as shown in the table, our method provides the potential to make a good trade-off between accuracy and latency. Specifically, when the iteration time is reduced to

# Iteration Times	NDS (%)	mAP (%)	Latency (ms)
1	67.1	63.4	87.7
2	71.9	69.3	94.2
4	73.1	70.7	99.8
6	<b>73.2</b>	<b>71.2</b>	115.2
8	72.7	70.3	119.2

Table S2. **Effect of iteration times of the multi-modal decoder.** The reported performance is compared on the nuScenes validation set. We exploit ResNet-50 as the image backbone network. The latency is evaluated on an NVIDIA A100 GPU.

4, our PoIFusion can still achieve the highest NDS (73.1%) and mAP (70.7%) among the compared methods presented in Table 1, and in the meantime run faster than the fastest competitor (*i.e.*, BEVFusion) presented in Table 3.

**Shared Parameters VS. Unshared Parameters** of the Multi-Modal Decoder. Since the multi-modal object decoder is iteratively applied multiple times, we can exploit either shared parameters or unshared parameters. The results of using shared parameters and unshared parameters are presented in Table S3. As shown in this comparison, these two models achieve comparable performance. Moreover, sharing parameters of the multi-modal object decoder makes a smaller model size. Therefore, we use shared parameters of the multi-modal decoder by default.

	NDS (%)	mAP (%)
Shared Parameters	73.2	<b>71.2</b>
Unshared Parameters	<b>73.3</b>	70.9

Table S3. **Shared versus unshared parameters** of the multi-modal object decoder. The models are evaluated on the nuScenes validation set, with ResNet-50 as the image backbone network.

**Training without the pretrained LiDAR encoder.** In our main experiment, we follow the training policy of most recent works [2, 5, 42, 67, 75], *i.e.*, starting with the model weight of pretrained TransFusion-L and training the fusion model for 6 epochs. Here, we further study whether our PoIFusion can also be trained without a pretrained TransFusion-L model. Specifically, in this experiment, we follow the training policy of CMT [69] that trains the fusion framework with 20 epochs, with only the pretrained image backbone network. The performance comparison between our PoIFusion and CMT is presented in Table S4. Please note that these two models are trained with the same training policy, backbone network, and input resolution (details are summarized in the caption of this table). As shown in the table, our PoIFusion achieves 72.3% NDS and 68.4% mAP without pretrained LiDAR encoder, outperforming CMT with the same input resolution and training policy by 1.5% NDS and 0.5% mAP. This experiment demonstrates

Method	NDS (%)	mAP (%)
CMT	70.8	67.9
PoIFusion (ours)	<b>72.3</b>	<b>68.4</b>

Table S4. **Training without a pretrained TransFusion-L model.** The compared models are trained with the same training policy and evaluated on the nuScenes validation set. Both models use ResNet-50 and VoxelNet as the backbone network, with image resolution set as  $800 \times 320$  and voxel size set as  $(0.1m, 0.1m, 0.2m)$ .

our PoIFusion works very well under various training policies, further exhibiting its potential to serve as a strong baseline for future research.

### C. Additional Qualitative Results

In our main manuscript, we only visualize two scenes due to the limitation of pages. Here, we add more qualitative examples in Figure S1 to help intuitively present the detection results of our method. From the visualized results, it can be seen that our proposed method is able to accurately detect 3D objects under complex road conditions.

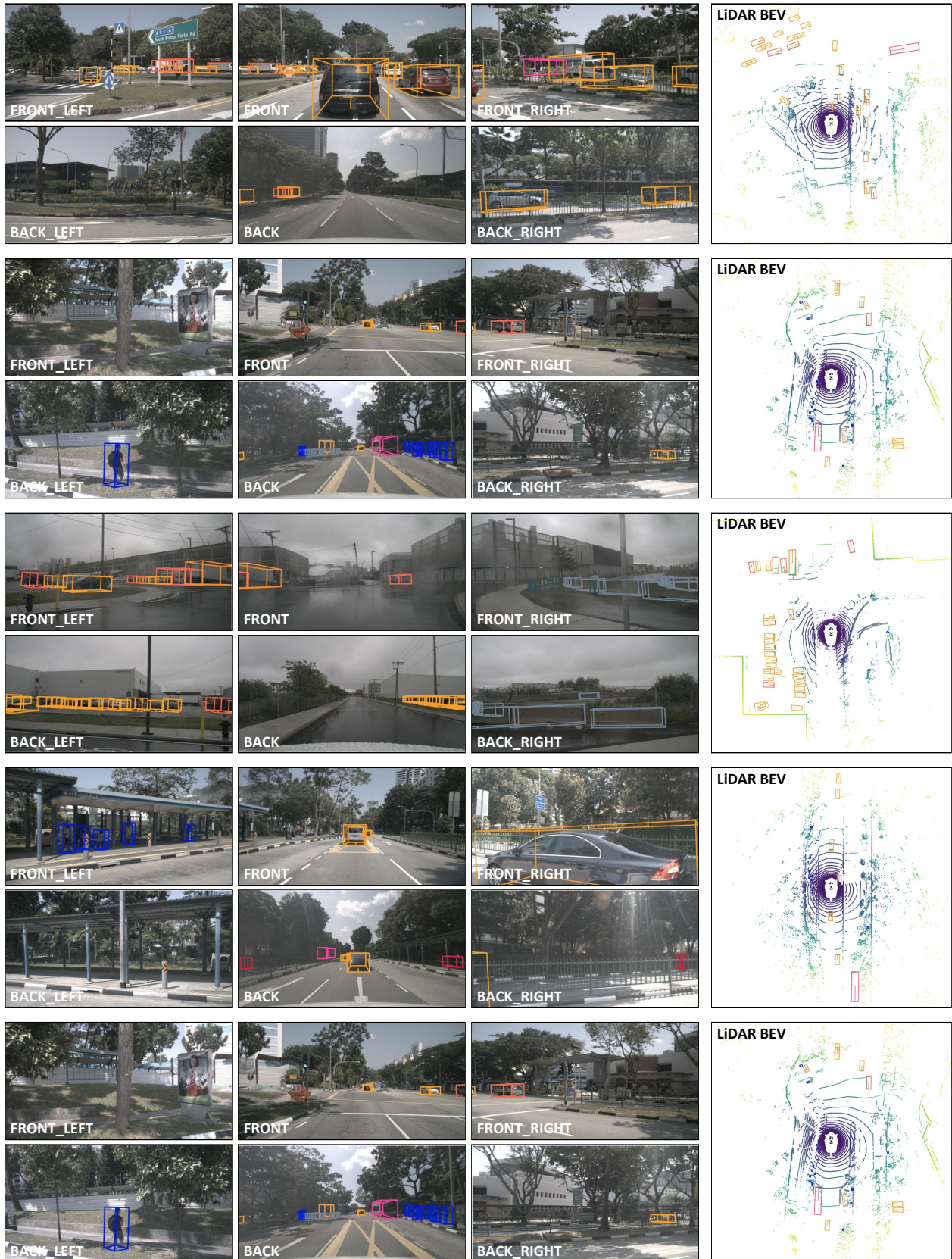


Figure S1. Supplement of Qualitative results on the nuScenes validation set.